Structure, permeability, and strength of a fault zone in the footwall of an oceanic core complex, the Central Dome of the Atlantis Massif, Mid-Atlantic Ridge, 30°N

Takehiro Hirose [a,*], Nicholas W. Hayman [b]

[a] Kochi Institute for Core Sample Research, JAMSTEC, 200 Monobe-otsu, Nankoku, Kochi 783-8502, Japan
[b] Institute for Geophysics, University of Texas, J.J. Pickle Research Campus, 10100 Burnet Road, Bldg. 196, Austin, TX 78758-4445, USA

ABSTRACT

Fault-zone samples recovered from 159 to 174 m below the seafloor (mbsf) in Hole 1309D from the Integrated Ocean Drilling Program (IODP) at the Atlantis Massif, Mid-Atlantic Ridge, 30°N, include both cataclastic and mylonitic fault rocks, and their gabbroic and ultramafic host rocks. Laboratory experiments determined the strength and permeability of nine fault-zone and host-rock samples with a triaxial apparatus under conditions that simulate present-day, *in situ* pressure conditions. The permeabilities of cataclasites are $\sim 10^{-18}$ m^2, while host-rock and mylonite permeabilities are $< 2 \times 10^{-19}$ m^2. When subjected to increasing differential stress, visible fractures increased the permeability of most rock types to $> 10^{-17}$ m^2. The strength of cataclasites is 260–380 MPa, weaker than that of mylonites of ~ 600 MPa. High resolution X-ray computed tomography (HRXCT) and optical microscopy shows that experimentally produced fractures preferentially form interconnected networks within cataclastic matrices. Thus, permeability and strength are a function of the fault-zone microstructure, which evolved during exhumation from upper mantle and lower crustal depths. Localization of cataclastic zones adjacent to altered ultramafic and mylonitic gabbroic rocks likely make the cataclastic portion of this fault a long-lived fluid conduit within the Atlantis Massif Oceanic core complex.

© 2008 Elsevier Ltd. All rights reserved.

1. Introduction

The most globally significant hydrothermal fluid circulation transports heat and solute through mid-ocean ridge systems, modifying the physical and chemical state of the oceanic crust (e.g., Alt et al., 1996). Fault zones within mid-ocean ridges provide essential fluid pathways, and therefore the permeability of fault zones may be one of the most important parameters that govern fluid circulation (Strens and Cann, 1982; Fisher, 1998; Fisher and Becker, 2000; Hayman and Karson, 2007). Important constraints on fault-zone permeability are the internal structures of fault zones and laboratory permeability measurements of fault-zone samples (Caine et al., 1996; Evans et al., 1997; Faulkner and Rutter, 2001; Wibberley and Shimamoto, 2003; Tsutsumi et al., 2004). However, most fault-rock studies focus primarily on samples from continental and fore-arc regions, and not mid-ocean ridges. Studies of mid-ocean ridge fault rocks can enhance our understanding of mid-ocean ridge faulting and fluid flow, and can also expand our understanding of the faulting process in general. For example,

detachment faults are important fluid conduits along slow-spreading ridges (Boschi et al., 2006; deMartin et al., 2007; McCaig et al., 2007). The structures and hydrothermal systems around detachment faults have an equally impressive topographic expression as comparable continental systems, and more pronounced seismicity, and heat and fluid flow.

This study focuses on a fault zone recovered from the Integrated Ocean Drilling Program (IODP) Hole 1309D in the Atlantis Massif, an oceanic core complex adjacent to the Mid-Atlantic Ridge (MAR) at ~ 30°N. The fault zone contains a variably deformed intrusive suite of gabbroic and ultramafic rocks, with both mylonites and cataclasites, all within a narrow interval between 159–173 m below the seafloor (mbsf). Site U1309 is on a detachment fault's footwall that was exhumed over the last 1–2 Ma (Blackman et al., 1998; Schroeder and John, 2004; Karson et al., 2006; Ildefonse et al., 2007). Studies of the detachment — where it is more completely exposed a few kilometers to the south of Hole 1309D — found a record of voluminous hydrothermal fluid flow (Boschi et al., 2006). Active venting today is recognized within the Lost City Field (LCF), a low-temperature, off-axis, vent field (Kelley et al., 2001; Früh-Green et al., 2003).

We experimentally determined the permeability of the fault zone from Hole 1309D by performing core-scale permeability measurements at pressure conditions that simulate the current

* Corresponding author.
E-mail addresses: hiroset@jamstec.go.jp (T. Hirose), hayman@ig.utexas.edu (N.W. Hayman).

depth of the fault zone, given the pressure of the water column and overlying crust (>20 MPa). We then evaluated the fracture permeability of fault rocks by conducting deformation experiments using a standard triaxial oil-medium apparatus. To interpret the experimental data, we studied the microstructure of the specimens using optical microscopy and high-resolution X-ray computerized tomography (HRXRT, or CT scanning). The geometry of the fractures varies with rock type leading to a contrast in the measured (experimental) syn-deformational permeability between samples.

The experimental results and petrographic observations illustrate that large increases in permeability proceed through a "crack-seal" (sensu lato) mechanism. In other words, fractures and cataclastic zones develop during increments of deformation, and, in nature, are subsequently sealed by hydrothermal minerals. However, because of heterogeneities in mineralogy and micro-structure, some parts of faults zones remain more permeable than other parts, even between intervals of deformation. For a variety of reasons that we discuss, our experimental data do not directly scale to nature, and thus do not place quantitative boundaries on fault strength and generally underestimate permeability, especially for deeper crustal conditions. However, the relative strengths and permeabilities, along with microstructural observations, explain the patterns of localization into cataclastic zones that were, and still are, important conduits for fluids through the Atlantis Massif.

2. Hole 1309D and the fault zone at 159–173 mbsf

The Atlantis massif is located ∼15 km west of the MAR, adjacent to the Atlantis transform (Fig. 1). Like many oceanic core complexes (OCCs) (Karson, 1999; Smith et al., 2006), the Atlantis massif has corrugations oriented perpendicular to the ridge axis, a serpentine-rich detachment system, and a massif dominated by gabbroic rocks (Blackman et al., 1998; Karson et al., 2006; Ildefonse et al., 2007). Hole 1309D is located along the northern surface of the central dome of the Atlantis Massif, ∼5 km north of the southern ridge where the detachment fault is best exposed (Blackman et al., 1998). The surface of the massif projects to the base of volcanics to the east, the hanging wall of the detachment. Recovery of core did not

begin until ∼20 mbsf, and — with the exception of loose pieces of talc-tremolite schist and basaltic breccias — quickly entered intrusive units that make up the footwall of the detachment.

Core recovery from Hole 1309D was >75% on average, and >50% in the fault zone between 159 and 173 mbsf, though a large interval between 168 and 172 mbsf was not recovered (Fig. 2). As with all drilling projects, we acknowledge that the recovered core represents a very censored view of the down-hole geology, and significant intervals of fault rocks were likely not recovered.

Hole 1309D contains many <10-m thick gabbroic and ultramafic units. Most of the units are cumulates of sill-like magmatic injections, but some could be residual lenses of mantle materials (Blackman et al., 2006; Ildefonse et al., 2007). The 159–173 mbsf fault zone localized within the gabbroic units adjacent to lenses of ultramafic rocks including serpentinized dunite and a troctolite that is pervasively altered to talc and tremolite (Fig. 3; Table 1).

In general, cores recovered from Hole 1309D do not have the high strain zones found at other localities such as the Southwest Indian Ridge (Dick et al., 2000). For example, using the numerical index of IODP structural geology logs, the 159–173 mbsf fault zone has a crystal plastic and cataclastic intensity of ∼"2", based on mesoscopic (hand sample) inspection with "0" representing undeformed rocks and "4" representing ultramylonites, ultra-cataclasites, or highly foliated magmatic shear zones (Fig. 2). The microstructure reflects the low "intensity" values, with no highly stretched or thoroughly comminuted grains.

Despite the low strain, the 159–173 mbsf fault zone developed with exhumation across the entire crust, and contains penetrative mylonitic fabrics with dynamically recrystallized plagioclase and pyroxene grains, all superposed on a magmatic foliation (Fig. 3a,b, e,f). Cataclastic shear zones and (Fig. 3g,h) surrounding damage zones (Fig. 3c,d) cut, but do not completely overprint, the mylonitic zones (Fig. 3e,f). The fine-grained portions of the cataclasites are dominated by actinolite (Fig. 3h; Table 1). Preliminary in-vestigations have recognized both a newly grown and mechanically incorporated population of amphibole grains in the cataclastic matrices (McCaig, personal communication). The altered troctolite and dunite do not contain evidence of mylonitization or cataclasis
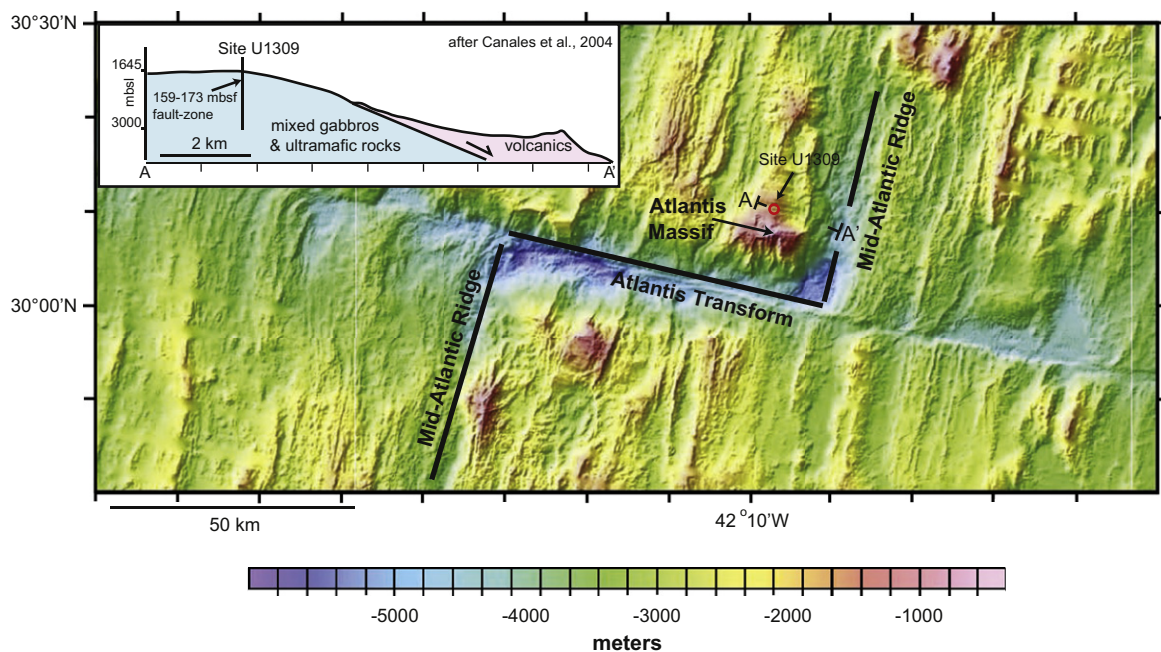

Fig. 1. Bathymetric map around the Atlantis Massif, Mid-Atlantic Ridge from the Marine Geoscience Data System (http://www.marine-geo.org/). Circle indicates drilling site of U1309. The very generalized cross-section on the map is oriented parallel to seismic line MEG-10 of Canales et al. (2004). "Fault zone" is the fault zone within basement rocks between 159 and 173 mbsf that we focus on here.
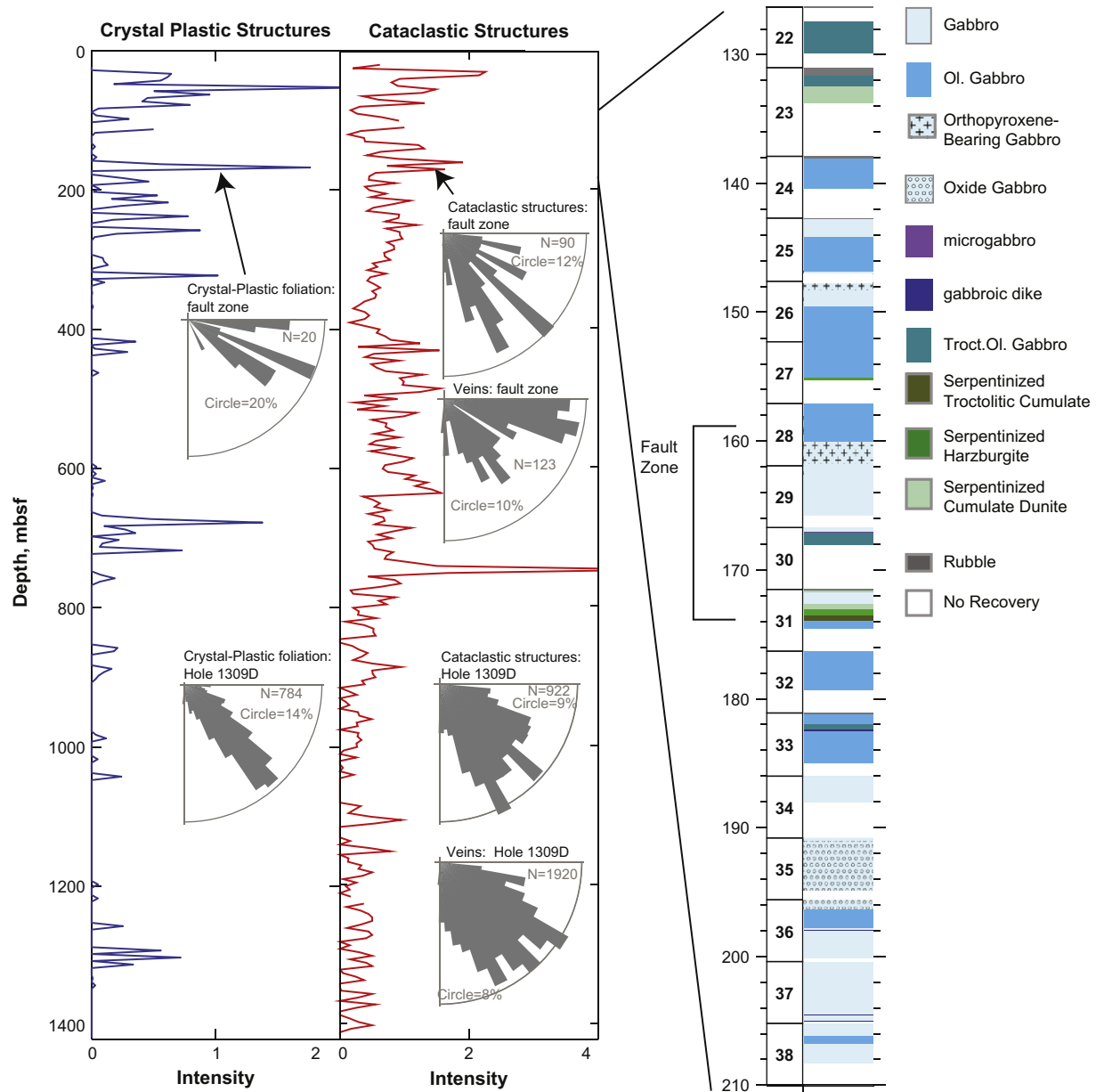
Fig. 2. Down-hole structure and lithology logs from the shipboard data (Blackman et al., 2006). Plastic and Cataclastic structure logs are based on hand-sample inspections and an assignment of a qualitative "deformation intensity" as explained in the text. Orientations of structures are only in the down-hole reference frame, and thus do not have azimuthal (geographic) information. The downhole lithology log for the interval surrounding the fault zone of interest (159–173 mbsf) is presented (lines indicate the depth interval for the log on the right side of the cataclastic structure log). Note that many intrusions with contrasting igneous textures and compositions are found within the same 100 m of the hole, indicating that the fault zone cut through a complicated igneous structure. Blank intervals indicate no recovery.

but olivine grains in the rocks are pervasively altered to serpentine (the dunite) and/or talc (the troctolite) (Fig. 3e,f; Table 1).

Most structures in Hole 1309D have moderate-to-steep dips in the "core reference frame"; azimuthal information is not available without further analysis of paleomagnetic and/or down-hole logging data (Fig. 2). Within the 159–173 mbsf fault zone the crystal plastic foliation and cataclastic shear zones have a shallower dip than elsewhere in the hole. Hydrothermal veins also have shallow and moderately steep dips, potentially forming a conjugate set about a shallowly dipping plane. The structural elements within the fault zone are thus inclined to the structures elsewhere in the hole indicating a local reorientation of principal stresses and/or tectonic rotations. The orientations also highlight the fault zone's potential role as a conduit for fluids moving transverse to the other dominant structural features.

3. Methods

3.1. Specimen preparations

Nine specimens were drilled with a 2.5-cm (1-inch) diameter bit from the working half of cores 28R to 31R (159–173 mbsf) in Hole 1309D (Table 2), and then polished into a cylindrical shape with a length of ~10 mm and diameter of 20 mm. Longer cylinders could have been made from select samples of intact host rocks, but this would have introduced size effects when comparing experimental results between rock types of different initial sample size. Thus, the specimens were short relative to other permeability and deformation experiments (e.g., Brace, 1984; Paterson and Wong, 2005). To eliminate pore water for gas permeability measurements, the specimens were dried at 80 °C in an oven for over 2 weeks until
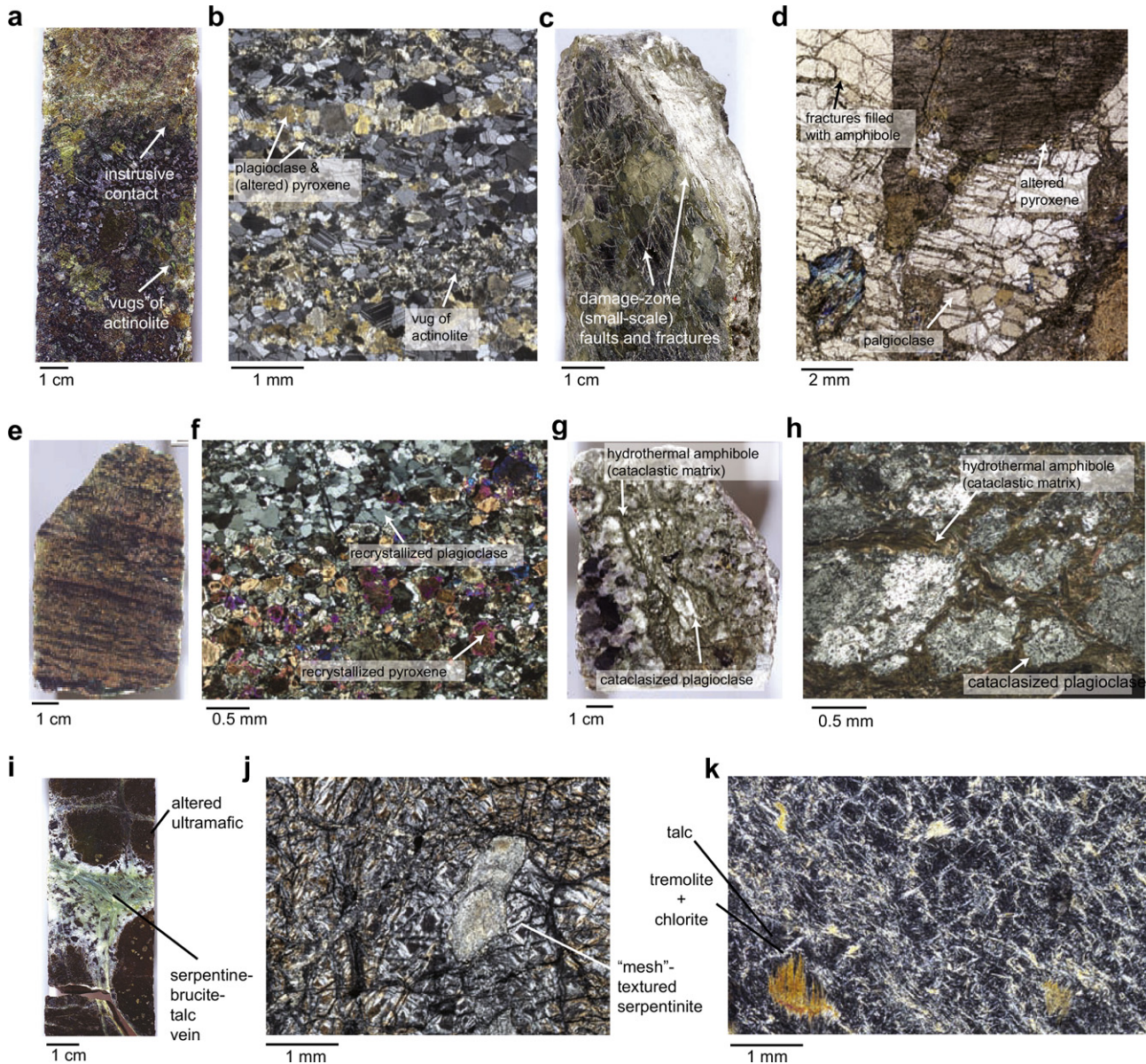
Fig. 3. (a) Core 28R1-30-45 above the fault zone studied here. A coarse-grained gabbro (lower portion) intruded a more mafic gabbro (upper portion, darker structure includes serpentinized olivine). (b) Sample 30R1-113-115 (in cross-polarized light): an undeformed gabbro with a magmatic foliation (note untwined plagioclase grains) located within the fault zone. More birefringent grains are amphibole grains that statically replaced pyroxene. (c) Core 29R1-70-75 near the top of the fault zone exhibits a talc shear zone that cuts coarse-grained gabbro. (d) 31R2-133-135 (partially cross-polarized light): damaged host rock at the base of the fault zone. (e) Core 30R1-107-115 from within the fault zone, exhibiting a mylonitic foliation. (f) 29R2-95-96 (in cross-polarized light): in the upper half of the fault zone, dynamically recrystallized plagioclase and pyroxene grains define crystal-plastic foliation. (g) Core 29R1-85-90 from within the fault zone, exhibiting an actinolite-rich cataclastic zone cutting a relatively felsic gabbro intrusion. (h) 29R1-85-87 (partially cross-polarized light): cataclasite in gabbro located in the upper half of the fault zone. The matrix minerals are dominantly amphibole. (i) Core 31R2-29-49 exhibiting a serpentine-rich shear zone cutting altered dunite. (j) 31R2-16-18 (cross-polarized light) with "mesh-textured" serpentinite, wherein serpentine minerals, magnetite, tremolite replaced olivine and pyroxene. (k) 31R2-58-60 talc and tremolite rich altered ultramafic (troctolite).

the weight of the specimens became constant. Each of the specimens was then placed between perforated stainless steel spacers, jacketed by three layers of polyolefin tube, and then put into an apparatus. To ensure that there was no flow between the polyolefin tubes and the specimen surface, we conducted a test with a dummy specimen of stainless steel: we imposed a pore pressure difference of 3 MPa between specimen ends at a confining pressure of 10 MPa, and confirmed that there was no pressure leak over ∼10 h.

3.2. Permeability and deformation experiments

The permeability and deformation experiments were performed using an intra-vessel oil-medium triaxial apparatus capable of independently controlling confining pressure, pore-fluid pressure and strain rate (Fig. 4). Permeability was determined at room temperature by using the steady-state flow method with nitrogen gas as a pore fluid. The steady-state flow method consists of imposing a known pore-pressure gradient across the specimen and measuring the resultant flow rate, which is proportional to permeability (e.g., Scheidegger, 1974). Permeability, k, for the nitrogen gas flow is given by the following equation based on Darcy's law:

$$k = \frac{2\eta L Q}{A} \frac{P_{\text{down}}}{P_{\text{up}}^2 - P_{\text{down}}^2}$$

where Q is the flow rate, A is the cross sectional area perpendicular to the flow direction, L is the specimen length parallel to the flow

Table 1
List of the sample with its mineralogy

Core	Section	Interval		Piece	Depth (mbsf)	Run number	Silicate mineralogy
28R	3	31	37	4	159.74	IVA720	Plagioclase, clino-and ortho-pyroxene, talc (<10%), chlorite (<5%), termolite (<5%)
29R	1	5	7	1	161.95	IVA723	Plagioclase, clino-and ortho-pyroxene, talc (<10%), chlorite (<5%), termolite (<5%)
	1	85	87	7	162.75	IVA725	Plagioclase, clinopyroxen, actinolite(<30%), secondary
	1	117	119	11	163.07	IVA751	Plagioclase, clinopyroxen, actinolite (<30%), secondary plagioclased (<10%)
	2	95	97	10	164.35	IVA750	Plagioclase, clino-and ortho-pyroxene, vugs of actinolite/tremolite and talc
30R	1	113	115	14	167.83	IVA729	Plagioclase, clino-and ortho-pyroxene, vugs of actinolite/tremolite and talc
31R	2	16	18	2	173.12	IVA748	Serpertine, tremolite
	2	58	60	3	173.54	IVA730	Talc, chlorite, tremolite, serpentine
	2	133	135	13	174.29	IVA747	Plagioclase, clinopyroxene, tremolite/actinolite (<35%), chlorite (<20%)

direction, η is the viscosity of the pore fluid, and P_{up} and P_{down} are the upper and lower end of pore pressures across the specimen. We use $\eta = 1.773 \times 10^{-5}$ Pa s for nitrogen gas at 20 °C temperature and 1 MPa pressure based on the NIST database. We do not consider possible effects of a pore pressure gradient on viscosity because viscosity variations are quite small (<0.04×10^{-5} Pa s) over the pore pressure range used in this study. One side of the specimen was connected to the atmosphere through a flow meter, and thus $P_{down} = 0.1$ MPa. Flow rates were measured at the downstream portion with float-type flow meters, with an accuracy of 2% (Fig. 4). The measurable flow rates range from 0.5 to 5000 ml/min, which roughly corresponds to permeabilities from 2×10^{-19} to 2×10^{-15} m^2 for our specimen size.

Each experiment was carried out in three steps: (1) the confining pressure was raised in a stepwise manner from 5 to 130 MPa with a permeability measurement at each (typically 20 MPa) pressure step, with a constant pore pressure of 2 MPa. Pressure was then decreased and permeability was measured after the flow rate became nearly constant for each step (results noted in the left column labeled "before" in Fig. 5). In cases where permeability could not be determined for the more impermeable specimens, the pressure was raised to 130 MPa in a single, initial pressure step after a single measurement at low pressure. (2) After the first pressure cycle of permeability measurements, confining and pore pressures were increased again and kept constant at 30 and 2 MPa, respectively. Then, specimens were deformed up to an axial strain of 8.3% with an axial displacement rate of 0.01 mm/min, corresponding to an axial strain rate of $\sim 8.5 \times 10^{-5}$ s^{-1}. (3) Finally, after the axial load was released, the permeability of the fractured specimens was measured in the same manner as in step (1) to evaluate the fracture permeability (results noted as "after" in left column in Fig. 5). In summary, permeability measurements were

performed under an isotropic pressure up to 130 MPa in step (1) and (3), and under a deviatoric stress (without a constant mean stress for each run) in step (2) after pre-confinement to an effective pressure of 128 MPa.

The axial displacement of the loading column was measured outside the pressure vessel (Fig. 4). Thus, the shear strain of each specimen was corrected using stress versus axial displacement data of the stainless pistons. We did not correct the data for the mechanical effect of the jacket strength and O-ring friction. As the length-to-diameter ratio of our specimen is small, strength data from this study is possibly >10% higher than that previously reported on the samples with >2.5 axial ratios (Paterson and Wong, 2005). Theory and experiments also indicate that shorter specimens have higher permeabilities (e.g., Walder and Nur, 1986). In addition, gas permeability is usually higher than water permeability by more than an order of magnitude because of physico-chemical interactions between the rock and pore fluid (Faulkner and Rutter, 2000; Tanikawa and Shimamoto, 2006). Therefore, the strength and permeability data should only be used for comparative purposes between the samples reported in this study.

4. Experimental results

In the pressure cycling experiments (steps (1) and (3), described in the Section 3), permeability decreases by nearly an order of magnitude with increasing effective pressure, to 128 MPa (left column in Fig. 5, see also Supplementary Material 1). The permeability is not fully recoverable with subsequent decreasing pressure, though some reversibility was observed. Fig. 6a summarizes the permeability distribution with depth before and after deformation at an effective pressure of 28 MPa and with the downward pressure cycle. The permeability of the host rocks

Table 2
List of the sample and experimental results

Core	Section	Interval		Piece	Depth (mbsf)	Run number	Fault rock type	Permeability[a]		Peak strength (MPa)	Total axial strain (%)
								Before (m^2)	After (m^2)		
28R	3	31	37	4	IVA720	159.74	Host rock (gabbro)	NA	4.IE−17	389	6.0
29R	1	5	7	1	IVA723	161.95	Damaged host rock (gabbro)	9.6E-19	8.0E−17	406	3.5
	1	85	87	7	IVA725	162.75	Cataclasite (gabbro)	2.2E-18	1.9E−17	272	7.8
	1	117	119	11	IVA751	163.07	Cataclasite (gabbro)	2.1E-18	5.3E−17	371	6.3
	2	95	97	10	IVA750	164.35	Mylonite (gabbro)	NA	8.8E−18	647	3.4
30R	1	113	115	14	IVA729	167.83	Mylonite (gabbro	NA	2.0E−17	598	3.6
31R	2	16	18	2	IVA748	173.12	Serpentinized dunite	NA	4.2E−17	263	6.9
	2	58	60	3	IVA730	173.54	Altered ultramafic	3.3E-19	4.0E−18	306	8.3
	2	133	135	13	IVA747	174.29	Host rock (gabbro)	NA	3.4E−17	362	5.7

[a] Permeability at effective pressure of 28 MPa at downward pressure cycle from confining pressure of 130 MPa.
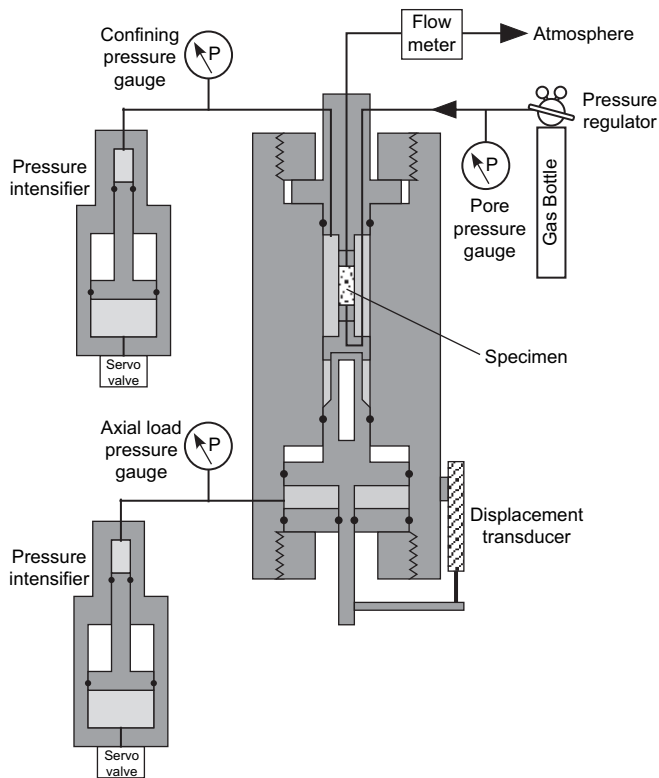
Fig. 4. Schematic diagram of the intra-vessel deformation and fluid flow apparatus. A steady-state flow method with nitrogen gas as a pore fluid was used to determine permeability. A constant pore pressure of 2 MPa was kept at the lower side of the specimen, while gas flow rate was measured at the upper side of the specimen.

(gabbro and serpentinized dunite) and mylonites is less than the lower limit of the measurement ($<2 \times 10^{-19}$ m^2), while that of cataclasites (IVA723, 725 and 751) is on the order of 10^{-18} m^2 and that of an altered ultramafic unit (IVA730) is 3×10^{-19} m^2. After axial deformation all of the specimens have a permeability of 10^{-18}–10^{-16} m^2 – up to 3 orders of magnitude higher than before deformation – at an effective pressure of 28 MPa with a downward pressure cycle (solid circles in Fig. 6a).

A representative plot of the permeability evolution during axial deformation is shown in Fig. 5b (IVA751). Up to an axial strain of 1.0% the permeability decreases gradually due to compaction and collapse of pores. When the differential stress reaches half of the peak value at an axial strain of $\sim$1.0%, the permeability increases rapidly with further axial strain. After the yielding or peak strength, the permeability of all of the specimens increases with continued axial strain. Although the axial strain at the peak differential stress varies with rock type, all specimens show a similar correlation between permeability and stress evolution with strain. An exception to the permeability evolution is run IVA748 on a serpentinized dunite; the permeability of the dunite increased after it yielded, but started to drop at the peak strength and then continuously increased again (Fig. 5d). Although the total axial strain and the deviatoric stress varies from run to run, all permeability data after the deformation range from 1×10^{-18} to 8×10^{-17} m^2.

The strength of the cataclasite specimens (IVA725 and 751) are 280 and 380 MPa at an effective pressure of 28 MPa, while their gabbroic host rocks (IVA720 and 747) and damaged host rock have strengths of 360–400 MPa, slightly stronger than those of cataclasites (Fig. 6b). In contrast, the mylonites (IVA729 and 750) are much stronger than the others by more than 200 MPa. Serpentinized dunite (IVA748) and altered ultramafics (IVA730) are weak (260 and 300 MPa in strength, respectively) and their stress–strain

curves are similar to that of the cataclasites (compare Fig. 5b and Fig. 5d,e). Both altered ultramafic and cataclasized gabbros have similar strengths, but the permeability of the altered ultramafics after axial deformation still remains $\sim$10^{-18} m^2, an order of magnitude lower than that of others at an effective pressure of 28 MPa with a downward pressure cycle (Fig. 6a).

5. Microstructure of experimentally deformed specimens

To facilitate interpretations of the experimental data, three-dimensional views of the experimentally deformed specimens are presented via HRXCT (Fig. 7). Scans were attained at the High-Resolution CT Facility at the University of Texas, Austin (see Ketcham and Iturrino, 2005 for a similar application of HRXCT and references therein for the development of the approach). Running at 210 kV and 0.1 mA, 1441 scans were attained of the nine post-deformation cylinders. The scans were stacked and rendered with Amira visualization software. The brightness of any voxel within the rendering is a function of the contrast in X-ray attenuation between phases, a function of density, atomic number, and the X-ray energy. For gabbroic specimens, brightest voxels tend to be oxides, next brightest are pyroxenes and/or amphiboles, and the least bright tend to be the plagioclase (Fig. 7a–c). Pore space and fractures are darker than the plagioclase, and have conspicuous geometries. Highly contrasting grains can be resolved to grain sizes of a few tens of micrometers. Fractures, however, are not easily studied at the micrometer scale because these structures cut across minerals with a range of attenuation properties. Here we focus on the general geometric characteristics of the experimental fractures at the sample scale, and their relationships with the surrounding natural microstructure.

In the experimentally deformed coarse-grained gabbro, fractures nucleated on the rim of specimen ends and propagated inward, and either tapered or splayed at grain boundaries (Fig. 7a). For coarse-grained specimens the fracture geometries are dominated by a single prominent fracture, though in the interior of the specimens numerous small-scale fractures form networks and splays surround the prominent fractures (e.g., 29R1-5-7, Fig. 7g). Shear offsets along the fractures are not visible in CT images and optical petrography reveals little shear deformation across experimentally produced fractures (Fig. 8a). Accordingly, coarse-grained gabbros have experimental fracture permeabilities between 10^{-16} and 10^{-17} m^2 during a pressure cycle (see left column in Fig. 5a). In contrast the mylonites contain fewer fractures that did not propagate directly into the specimen interior, but rather closely follow the outer boundary of the specimen (Fig. 7f). Thus, the experimental fracture permeability of these specimens is relatively low, between 10^{-17} and 10^{-18} m^2 (see left column in Fig. 5c).

In contrast with the mylonites and gabbroic specimens, cataclasites, serpentinite, and altered ultramafic specimens contain networks of fractures with numerous splays and anastamosing geometries (Fig. 7a–e). In cataclasites, fractures tend to follow the natural cataclastic matrix (Fig. 8b). Even though these specimens have qualitatively similar fracture patterns, their permeabilities are variable. For example, the altered ultramafic specimen has a much lower permeability ($\sim$10^{-18} m^2 at an effective pressure of 28 MPa during the depressurization cycle) than the other specimens (Fig. 6a). Clearly, the dense and complicated array of fractures in this specimen (31R2-58-60, Fig. 7e) did not significantly increase its permeability relative to other specimens. In contrast, serpentinized dunite is quite permeable, $\sim$5 $\times$ 10^{-17} m^2 at an effective pressure of 28 MPa during the depressurization cycle (Fig. 6a). Lastly, cataclastic specimens such as 29R1-85-87 (Fig. 7c) and 29R1-117-119 (Fig. 7d), start out with similar permeabilities, but their fracture permeabilities are different after axial deformation (Fig. 5c,d). We hypothesize further on the controls on, and implications of,
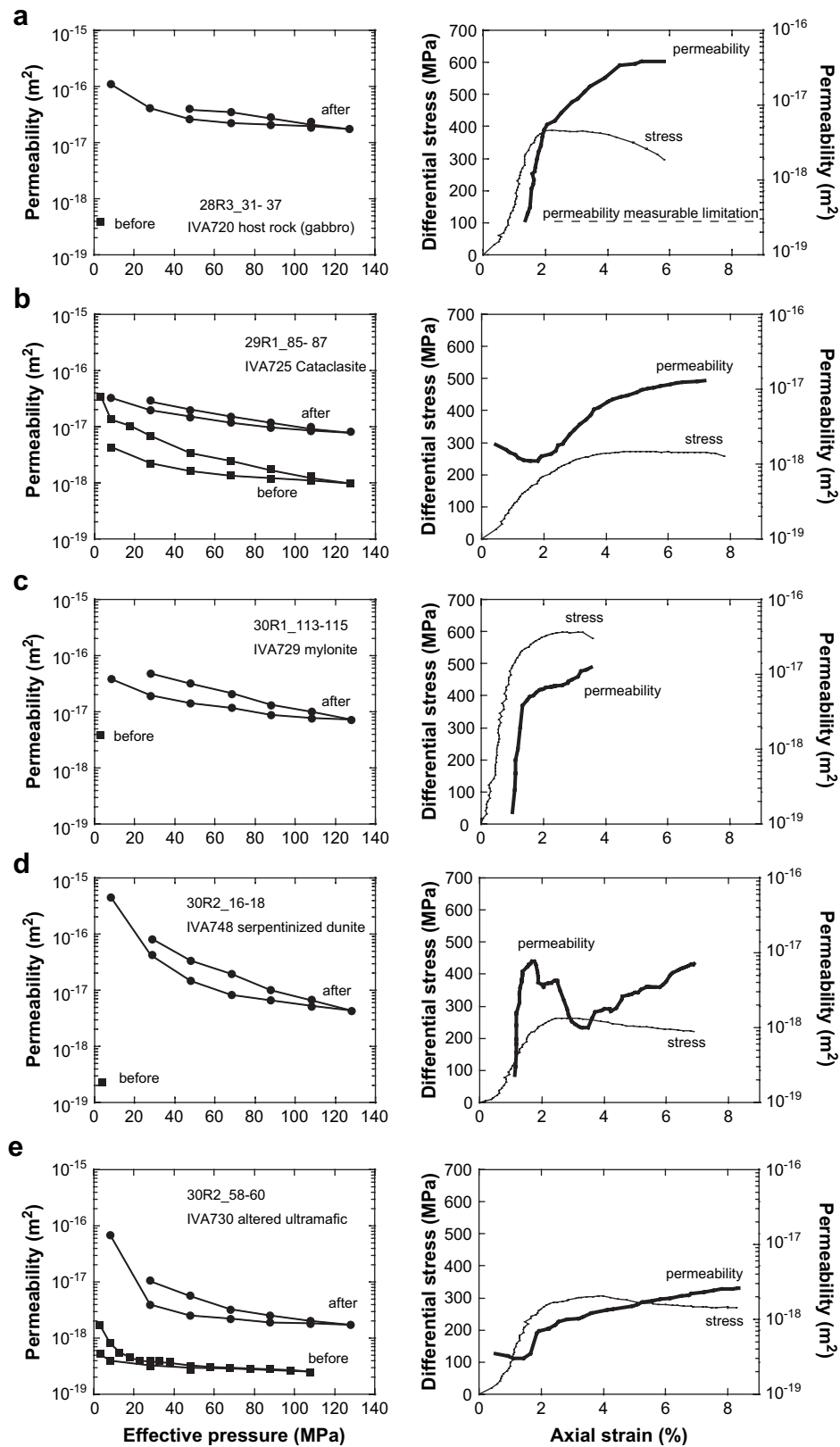
Fig. 5. Representative experimental data for the permeability evolution as a function of axial strain (right column), and the permeability response to an increasing effective pressure of up to 128 MPa (left column) for specimens collected across the major fault zone from 159 to 173 mbsf in Hole 1309D. Deformation experiments were performed at an effective pressure of 28 MPa. Permeability values before and after deformation were plotted as squares and circles, respectively, in the left column. In the case that permeability could not be determined for the impermeable specimens (i.e., a, c and d), pressure was raised to 130 MPa after a permeability measurement at low pressure. Errors of measurement are within the size of data point (see also Supplementary Material 1).
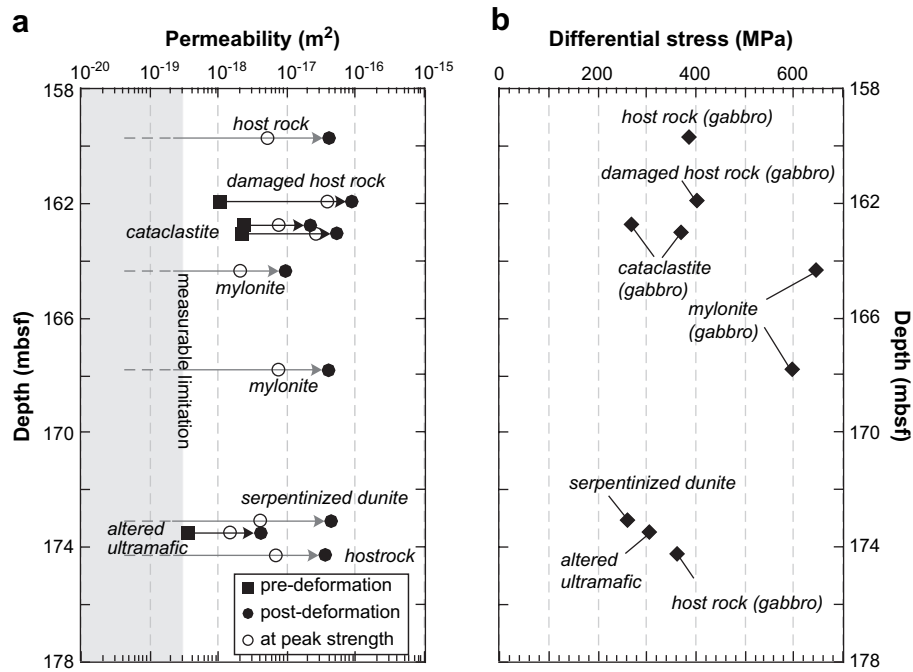
Fig. 6. (a) Distribution of measured permeabilities before and after deformation with depth in mbsf. Solid squares and circles are data of pre- and post-deformation, respectively, measured under isotropic pressure of 30 MPa and pore pressure of 2 MPa during downward pressure cycle from 130 MPa confining pressure. Open circles indicating permeability values at peak strength during deformation. Note that stress state (mean stress) is different with each open-circle data. Pre-deformation permeabilities for five impermeable specimens were lower than measurable limit of the measurement. (b) Peak strength of nine specimens at effective pressure of 28 MPa as a function of depth in mbsf.

strength and permeability contrasts between the samples in the following discussion.

6. Discussion

Fault zones in both continental and ocean crust have relatively impermeable, high-strain fault core surrounded by a relatively permeable, low-strain damage zone (Caine et al., 1996; Hayman and Karson, 2007; Mizoguchi et al., 2008). The fault zone focused on here contains multiple lithologies, fault-rock types, and variable amounts of strain and alteration. Thus, a more detailed description of how permeability varies across the fault zone is required. Such complex structures of fault zones have been described in continental faults (Faulkner et al., 2003; Wibberley and Shimamoto, 2003), but not in *in situ* oceanic faults before now.

We have a fairly straightforward interpretation of the controls on strength and permeability *at low confining pressures* (i.e. 30 MPa). Undeformed host rocks and mylonites are very crystalline with few cracks, matrix minerals, or interstitial pores (Fig. 3a,b, e,f). Thus, these specimens are very strong (>360 to >600 MPa) and impermeable ($<10^{-19}$ m^2). In contrast, damaged gabbros and cataclasites are *relatively* permeable ($>10^{-18}$ m^2) with variable strengths (Fig. 6). The properties of the damaged and cataclastic rocks are due to the fine-grained matrix minerals and natural fractures. Mineralogic controls on permeability and strength are also important. For example, talc and serpentine make the ultramafic rocks impermeable ($<10^{-18}$ m^2) but weaker than the host rocks and mylonites.

The strain–permeability response *during axial deformation* also contrasts between samples. Undeformed and damaged coarse-grained gabbros and cataclasites have a very monotonic strain response with an equally simple permeability evolution (e.g., Fig. 5b). Mylonites also have a simple, monotonic strain and permeability evolution with stress, but reach peak strength relatively quickly, with axial strains of ~3% (Fig. 5c). In contrast, ultramafic rocks rich in talc-tremolite or serpentine either have very complicated permeability

and strain responses (serpentinized dunite, IVA748, Fig. 5d), or have somewhat flat responses (altered ultramafic, IVA730, Fig. 5e). These ultramafic specimens have roughly the same peak strength as other cataclasites. Indeed, the serpentinized dunite and one of the cataclasites are equally the weakest within the fault zone (<300 MPa) (Fig. 6). Yet, once experimentally fractured, the permeability of all of the fault-zone specimens become similar within an order of magnitude (10^{-17}–10^{-16} m^2). A key exception is the altered ultramafic unit, which retains its low permeability despite the abundance of experimentally induced fracture.

We can estimate the microstructural and mineralogic controls on the samples' strain–permeability responses to experimental deformation. The cataclastic matrix of actinolite, chlorite, and comminuted material is relatively weak and localizes fractures. Natural microfractures in damage-zone materials cause similar strain–permeability responses as the cataclastic rocks (e.g., Uehara and Shimamoto, 2004). In contrast, the crystalline microstructures and igneous mineralogy of the host rock and mylonites inhibits fracturing and lowers resulting fracture permeability. More subtle differences within the range of permeabilities are primarily due to the microstructure of the fractures: wide, through-going fractures cause higher permeabilities than networks of thinner, discontinuous fractures. Lastly, we hypothesize that the ultramafic rocks are weak but impermeable during deformation because even though fractures can easily develop in the weak talc-rich rock, they are not able to propagate through the material and remain as wide fluid conduits (Fig. 8c). The talc-serpentine mineralogy likely has some plasticity that restricts fracture permeability, even at low stress and strain.

The strength–permeability behaviors in our experiments are difficult to relate to nature. Core-scale measurements here and in previous studies (e.g. Johnson, 1980a,b) are much lower than *in situ* borehole measurements (10^{-18}–10^{-13} m^2) and numerical models of heat and fluid flow around flanks (10^{-16}–10^{-9} m^2) (see references in Fisher, 1998). This marked difference between field- and core-scale measurements is often explained by fractures (e.g., Brace, 1980). Fractured samples are not usually collected for laboratory
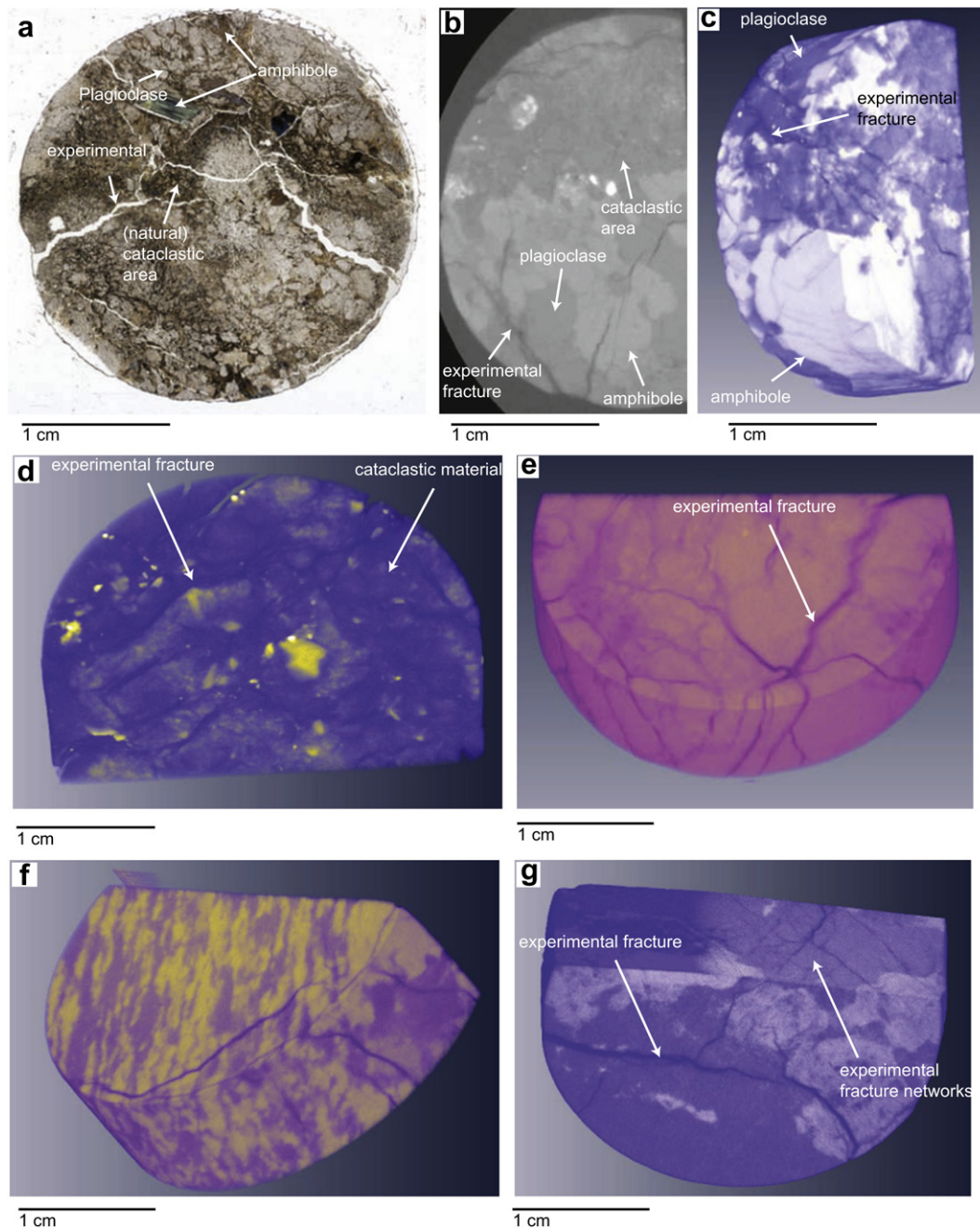
Fig. 7. (a) 29R1-85-87 (run IVA725), a thin-section scan illustrating the centimeter-scale structure of experimental fractures that propagated into cataclastic portions of the sample. (b) 29R1-117-119 (run IVA751), a single slice from a CT scan of a cataclastized gabbro, with a comparable view to the thin section in 'a'. (c) 29R1-117-119 (run IVA751), a three-dimensional rendering of the CT scan of 'b'. (d) 29R1-85-87 (run IVA725): Cataclasite from within the fault zone. Note that the sample is matrix dominated, and a dense network of interconnected experimentally produced fractures fills the sample. (e) 31R2-58-60 (run IVA730): altered ultramafic from the lower part of the fault zone. Fractures are thin, and form a complex network in a relatively continuous material. (f) 30R1-113-15 (run IVA729): a mylonite from within the fault zone; note how experimental fractures nucleated along the sample boundary but did not propagate inward. (g) 29R1-5-7 (run IVA723): a gabbro from the top of the fault zone cut by an experimentally induced fracture set.

permeability measurements due to difficulties in recovery and sample treatment. Additionally, borehole and surface measurements of heat flow could reflect more permeable fault-zone materials that were not recovered (see gaps in core recovery in Fig. 2). Despite issues of recovery, we argue that the permeability difference between field- and core-scale measurements is mostly due to the scale dependence of fracture permeability (e.g., Neuman and Di Federico, 2003). As fracture permeability is primary controlled by aperture and connectivity of fractures, a future experimental routine could be developed to scale fracture permeability to field-scale fluid and heat flow measurements (e.g., Renshaw and Park, 1997).

Another challenge to relating the laboratory measurements to nature is that the fault zone is the product of a >1 Ma history involving intrusions of magma, alteration by high-temperature hydrothermal fluids, and plastic and frictional deformation under evolving pressure–temperature conditions. Observations of active hydrothermal systems along the MAR suggest that deeply rooted faults remain fluid conduits throughout their history. The Trans-Atlantic Geothermal (TAG) field and massive sulfide deposit at 26°N overlies a detachment that undergoes incredibly high rates of seismicity, 19,232 microearthquakes over 8 months (deMartin et al., 2007). The seismicity extends to ~7000 mbsf, and defines
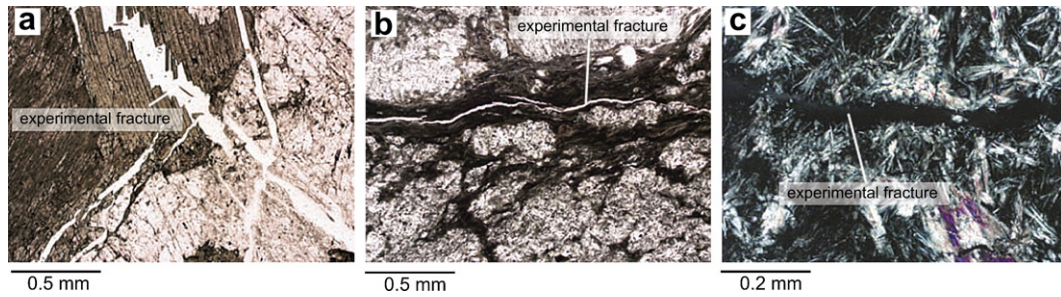
Fig. 8. Photomicrographs of thin sections showing typical experimental fractures. (a) 29R1-117-119, cataclasite (run IVA751). (b) 29R1-85-87, cataclasite (run IVA725). Experimental fractures tend to cut through the natural cataclastic matrix. (c) 31R2-58-60, altered ultramafic (run IVA730).

adjacent antithetic normal faults in the detachment footwall to ~4000 mbsf. Along the Atlantis Massif, the Lost City Field (LCF) is localized by footwall faults (Kelley et al., 2005). However, the footwall faults exposed along the Atlantis Massif are not recently active; pelagic sediment unconformably overlies the faults (Karson et al., 2006). The two examples of TAG and the LCF show that coseismic fluid flow occurs across many crustal conditions, and that flow continues through relatively inactive faults.

The experiments discussed here cannot directly bear on the deeper crustal history of such ocean crustal faults. The experiments do, however, suggest some mechanisms for changing permeability, strength, and slip behavior over time (Fig. 9). For example, the experimental generation of fracture permeability is potentially analogous to how permeability changes within a fault zone during coseismic fluid pressure fluctuations (Sibson, 1981). Fault zones that are permeable during earthquakes can then become sealed during the interseismic periods due to the effects of mineralization and compaction (i.e., Fig. 5b shows that permeability of cataclastic samples decreases at the onset of the differential stress increase). We thus propose that "cycles" of seismic and interseismic deformation largely drive the most voluminous phases of fluid flow.

The TAG and LCF, and mid-ocean ridge hydrothermal systems in general, exhibit diverse and extraordinary temporal and spatial scales of seismicity and hydrothermal activity, as well as variable geologic structure. Our conceptual model (Fig. 9) suggests that such diversity may be partly due to fault structure. For example, talc and serpentine within parts of a fault zone can weaken the fault and stabilize slip (i.e., Moore and Rymer, 2007) while decreasing permeability temporarily (Fig. 5d). Such alteration (and potentially deformation) of ultramafic materials can proceed at the same time as strain localization and fluid flow in adjacent amphibole-bearing cataclasites. Because more permeable cataclasites and damage zones surround less permeable rocks, fault-focused fluid flow can continue even after intervals of coseismic fault slip cease. Such patterns of permeability and strength in the samples from the IODP 1309D core thus inform a conceptual model for the intriguing and impressive patterns of seismicity and fluid flow observed along the MAR.

7. Conclusion

A fault zone recovered from 159 to 174 mbsf in Hole 1309D at the Atlantis Massif, Mid-Atlantic Ridge, 30°N is composed of both cataclastic and mylonitic fault rocks, damaged gabbros, and host rocks of both unaltered gabbro and highly altered ultramafic rocks. The permeability of cataclasites are $\sim 10^{-18}$ m^2, while host rocks and mylonites are $<2 \times 10^{-19}$ m^2 at confining and pore pressures of 30 and 2 MPa, respectively, and a downward pressure cycle from
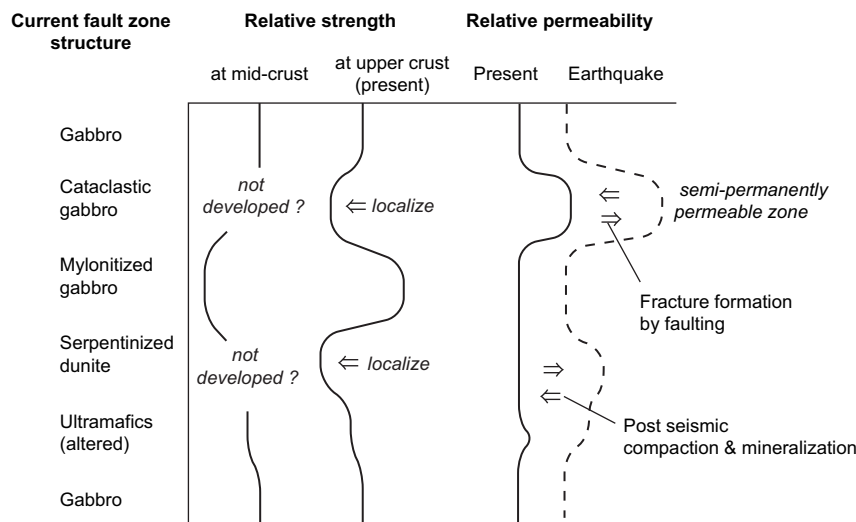

Fig. 9. Graphical illustration of the evolution of strength and permeability with fault slip at different crustal conditions. The mylonite was relatively weak at middle crustal conditions, but became quite strong and impermeable in the upper crust. Strength data (Fig. 6b) indicate that cataclasites, altered ultramafics, and serpentinized dunite, are weaker than other units at upper crustal conditions. Thus, strain localized and eventually formed fractures in these weaker zones, potentially during seismic slip and coseismic fluid flow. As permeability increased with strain, preferentially within cataclastic zones and the serpentinized dunite, these localized zones became more permeable than the surrounding fault zone and host rock (dotted line). However, talc-serpentine rich rocks tended to stabilize slip, further localizing strain into the adjacent cataclasite. Moreover, damaged host rock and one of the cataclasite became more permeable at peak strength but at lower strains than the others (open circle in Fig. 6a). Even during interseismic and postseismic intervals, the cataclastic and damage zones remained more permeable than the surrounding rocks.

confining pressure of 130 MPa (nearly *in situ* pressure conditions). This implies that the cataclastic zone is a dominant fluid pathway for the current fluid circulation in this mature fault zone. However, once visible fractures developed by axial deformation at a confining pressure of 30 MPa, permeability of all the specimens increases independently of rock type to $\sim 10^{-17}$ m^2. An exception is a talc-rich ultramafic sample which retains a permeability of 2×10^{-18} m^2 even after an axial strain of 8.3%.

Strength data of samples recovered from the fault zone indicate that cataclasites and ultramafics are weaker than others, and that mylonites are much stronger than the host gabbro. This implies that, once in the upper crust, strain must localize into the cataclastic and ultramafic zones. However, the samples of ultramafic units are free of cataclastic or mylonitic microstructures, and some altered ultramafic units remain relatively impermeable even during experimental deformation. Thus, cataclastic zones within the fault zone localized *adjacent* to the ultramafic units and older mylonitic shear zones. Once developed, the cataclastic zones likely acted as a permeable zone in the fault zone throughout coseismic exhumation of the oceanic core complex from the lower crust, a process currently operating at the Trans-Atlantic Geothermal field to the south. Additionally, the permeability contrasts between parts of the fault zone allow the fault to serve as a longer-lived conduit, potentially in a similar manner to what is currently observed on the Lost City Field.

Acknowledgments

Appendix A. Supplementary data

Supplementary data associated with this article can be found in the online version, at doi:10.1016/j.jsg.2008.04.009.

References

Alt, J.C., Laverne, C., Vanko, D., Tartarotti, P., Teagle, D.A.H., Bach, W., Zuleger, E., Erzinger, J., Honnorez, J., Pezard, P.A., Becker, K., Salisbury, M.H., Wilkens, R.H., 1996. Hydrothermal alteration of a section of upper oceanic crust in the eastern equatorial Pacific: a synthesis of results from Site 504 (DSDP Legs 69, 70, and 83, and ODP Legs 111, 137, 140, and 148). In: Alt, J.C., Kinoshita, H., Stokking, L.B., Michael, P.J. (Eds.), Proceedings of the Ocean Drilling Program, Scientific Results, vol. 148. College Station, TX, pp. 417–434.

Blackman, D.K., Cann, J.R., Janssen, B., Smith, D.K., 1998. Origin of extensional core complexes: evidence from the Mid-Atlantic Ridge at Atlantis Fracture Zone. Journal of Geophysical Research 103, 21315–21333, doi:10.1029/98JB01756.

Blackman, D.K., Ildefonse, B., John, B.E., Ohara, Y., Miller, D.J., MacLeod, C.J., Expedition 304/305 Scientists, 2006. Proceedings of the Integrated Ocean Drilling Program, vol. 304/305. Integrated Ocean Drilling Program Management International, Inc., College Station, TX, doi: 10.2204/iodp. proc.304305.

Boschi, C., Fruh-Green, G.L., Delacour, A., Karson, J.A., Kelley, D.S., 2006. Mass transfer and fluid flow during detachment faulting and development of an oceanic core complex, Atlantis Massif (MAR 30°N). Geochemistry, Geophysics, Geosystems 7, doi:10.1029/2005GC001074.

Brace, W.F., 1980. Permeability of crystalline and argillaceous rocks. International Journal of Rock Mechanics and Mining Sciences 17, 241–251.

Brace, W.F., 1984. Permeability of crystalline rocks-new insitu measurements. Journal of Geophysical Research 89, 4327–4330.

Caine, J.S., Evans, J.P., Forster, C.B., 1996. Fault zone architecture and permeability structure. Geology 24, 1025–1028.

Canales, J.P., Tucholke, B.E., Collins, J.A., 2004. Seismic reflection imaging of an oceanic detachment fault: Atlantis megamullion (Mid-Atlantic Ridge, 30°10′N). Earth and Planetary Science Letters 222, 543–560.

deMartin, B.J., Canales, R.A.R., Canales, J.P., Humphris, S.E., 2007. Kinematics and geometry of active detachment faulting beneath the Trans-Atlantic Geotraverse (TAG) hydrothermal field on the Mid-Atlantic Ridge. Geology 35, 935–938.

Dick, H.J.B., et al., 2000. A long in situ section of the lower oceanic crust: results of ODP Leg 176 drilling at the Southwest Indian Ridge. Earth and Planetary Science Letters 179, 31–51.

Evans, J.P., Forster, C.B., Goddard, J.V., 1997. Permeability of fault-related rocks, and implications for hydraulic structure of fault zones. Journal of Structural Geology 19, 1393–1404.

Faulkner, D.R., Rutter, E.H., 2000. Comparisons of water and argon permeability in natural clay-bearing fault gouge under high pressure at 20 degrees C. Journal of Geophysical Research 105, 16415–16426.

Faulkner, D.R., Rutter, E.H., 2001. Can the maintenance of overpressured fluids in large strike-slip fault zones explain their apparent weakness? Geology 29, 503–506.

Faulkner, D.R., Lewis, A.C., Rutter, E.H., 2003. On the internal structure and mechanics of large strike-slip fault zones: field observations of the Carboneras fault in southeastern Spain. Tectonophysics 367, 235–251.

Fisher, A.T., 1998. Permeability within basaltic oceanic crust. Reviews of Geophysics 36, 143–182.

Fisher, A.T., Becker, K., 2000. Channelized fluid flow in oceanic crust reconciles heat-flow and permeability data. Nature 403, 71–74.

Früh-Green, G.L., Kelley, D.S., Bernasconi, S.M., Karson, J.A., Ludwig, K.A., Butterfield, D.A., Boschi, C., Proskurowski, G., 2003. 30,000 years of hydrothermal activity at the Lost City vent field. Science 301, 495–498.

Hayman, N.W., Karson, J.A., 2007. Faults and damage zones in fast-spread crust exposed on the north wall of the Hess Deep Rift: conduits and seals in seafloor hydrothermal systems. Geochemistry, Geophysics, Geosystems 8, Q10002,, doi: 10.1029/2007GC001623.

Ildefonse, B., Blackman, D.K., John, B.E., Ohara, Y., Miller, D.J., MacLeod, C.J., Integrated Ocean Drilling Program Expeditions 304/305 Science Party, 2007. Oceanic core complexes and crustal accretion at slow-spreading ridges. Geology 35, 623–626.

Johnson, D.M., 1980a. Crack distribution in the upper oceanic crust and its effects upon seismic velocity, seismic structure, formation permeability, and fluid circulation. Proceedings of the Ocean Drilling Program, Initial Reports, vol. 51–53. College Station, TX, pp. 1479–1490.

Johnson, D.M., 1980b. Fluid permeability of oceanic basalts. Proceedings of the Ocean Drilling Program, Initial Reports, vol. 51–53. College Station, TX, pp. 1473–1477.

Karson, J.A., 1999. Geological investigation of a lineated massif at the Kane Transform Fault: implications for oceanic core complexes. Philosophical Transactions of the Royal Society of London Series A-Mathematical Physical and Engineering Sciences 357, 713–736.

Karson, J.A., Früh-Green, G.L., Kelley, D.S., Williams, E.A., Yoerger, D.R., Jakuba, M., 2006. Detachment shear zone on the Atlantis Massif Core Complex, Mid-Atlantic Ridge 30°N. Geochemistry, Geophysics, Geosystems 7, Q06016, doi:10.1029/2005GC001109.

Kelley, D.S., et al., 2001. An off-axis hydrothermal vent field near the Mid-Atlantic Ridge at 30°N. Nature 412, 145–149.

Kelley, D.S., et al., 2005. A serpentinite-hosted ecosystem: The Lost City Hydrothermal Field. Science 307, 1428–1434.

Ketcham, R.A., Iturrino, J.G., 2005. Nondestructive high-resolution visualization and measurement of anisotropic effective porosity in complex lithologies using high-resolution X-ray computed tomography. Journal of Hydrology 302, 92–106.

McCaig, A.M., Cliff, R.A., Escartin, J., Fallick, A.E., MacLeod, C.J., 2007. Oceanic detachment faults focus very large volumes of black smoker fluids. Geology 35, 935–938.

Mizoguchi, K., Hirose, T., Shimamoto, T., Fukuyama, E., 2008. Internal structure and permeability of the Nojima fault, southwest Japan. Journal of Structural Geology 30, 513–524.

Moore, D.E., Rymer, M.J., 2007. Talc-bearing serpentinite and the creeping section of the San Andreas fault. Nature 448, 795–797.

Neuman, S.P., Di Federico, V., 2003. Multifaceted nature of hydrogeologic scaling and its interpretation. Reviews of Geophysics 41, 1014.

Paterson, M.S., Wong, T.-F., 2005. Experimental Rock Deformation – The Brittle Field. Springer-Verlag, Berlin, Heidelberg, New York.

Renshaw, C.E., Park, J.C., 1997. Effect of mechanical interactions on the scaling of fracture length and aperture. Nature 386, 482–484.

Scheidegger, A.E., 1974. The Physics of Flow Through Porous Media. University of Toronto Press, Toronto, Canada.

Schroeder, T., John, B.E., 2004. Strain localization on an oceanic detachment fault system, Atlantis Massif, 30°N, Mid-Atlantic Ridge. Geochemistry, Geophysics, Geosystems 5, doi:10.1029/2004GC000728.

Sibson, R.H., 1981. Fluid flow accompanying faulting; field evidence and models. In: Simpson, D.W., Richards, P.G. (Eds.), Earthquake Prediction: An International Review. American Geophysical Union Maurice Ewing Series, vol. 4, pp. 593–603.

Smith, D.K., Cann, J.R., Escartin, J., 2006. Widespread active detachment faulting and core complex formation near 13 degrees N on the Mid-Atlantic Ridge. Nature 442, 440–443.

Strens, M.R., Cann, J.R., 1982. A model of hydrothermal circulation in faults zones at mid-ocean ridge crests. Geophysical Journal of the Royal Astronomical Society 71, 225–240.

Tanikawa, W., Shimamoto, T., 2006. Klinkenberg effect for gas permeability and its comparison to water permeability for porous sedimentary rocks. Hydrology and Earth System Sciences Discussions 3, 1315–1338.

Tsutsumi, A., Nishino, S., Mizoguchi, K., Hirose, T., Uehara, S., Sato, K., Tanikawa, W., Shimamoto, T., 2004. Internal and permeability structures of the Neodani fault, Nobi active fault system, central Japan. Tectonophysics 379, 93–108.

Uehara, S., Shimamoto, T., 2004. Gas permeability evolution of cataclasite and fault gouge in triaxial compression and implications for changes in faultzone permeability structure through the earthquake cycle. Tectonophysics 378, 183–195.

Walder, J., Nur, A., 1986. Permeability measurement by the pulse-decay method: effect of poroelastic phenomena and non-linear pore pressure diffusion. International Journal of Rock Mechanics and Mining Sciences 23, 225–232.

Wibberley, C.A.J., Shimamoto, T., 2003. Internal structure and permeability of major strike-slip fault zones: the Median Tectonic Line in Mie Prefecture, Southwest Japan. Journal of Structural Geology 25, 59–78.